World Electric Vehicle Journal

MDPI

Article

Integrated Charger-Inverter for High-Performance Electric Motorcycles

Vu Tran Tuan [1,*], Matheepot Phattanasak [2] and Sangkla Kreuawan [3]

[1] School of Electrical Engineering, Hanoi University of Science and Technology, Hanoi 11615, Vietnam
[2] Department of Teacher Training in Electrical Engineering, King Mongkut's University of Technology North Bangkok, Bangkok 10800, Thailand; matheepot.p@fte.kmutnb.ac.th
[3] Real BPM Co., Ltd., Samutsakorn 74000, Thailand; sk@realbpm.co.th
* Correspondence: vu.trantuan@hust.edu.vn; Tel.: +84-2438-693-796

Abstract: A high-performance electric motorcycle (HPEM) integrated charger-inverter (ICI) with an induction motor (IM) is proposed in this article. Typical components are shared in drive and charge modes, resulting in savings of weight, volume, and cost. A two-stage ICI for AC induction motor powertrain with power factor correction (PFC) and battery charger functions is considered. Despite high voltage ripple on the DC link, a high bandwidth nonlinear controller can reject such a drawback and adequately provide a constant current or constant voltage charging process. The simulation results of 7 kW ICI are provided to validate the effectiveness and feasibility of the proposed system. Finite element analysis (FEA) determines the torque and losses of IM in charging mode.

Keywords: electric motorcycle; on-board charger; active filter; asynchronous (induction) motor; finite element analysis

Citation: Tuan, V.T.; Phattanasak, M.; Kreuawan, S. Integrated Charger-Inverter for High-Performance Electric Motorcycles. *World Electr. Veh. J.* **2021**, *12*, 19. https://doi.org/10.3390/wevj12010019

Received: 11 November 2020
Accepted: 27 January 2021
Published: 1 February 2021

1. Introduction

In electric vehicles (EVs) application, driving range is one of most important criteria determining whether people will buy an EV. Both battery technology and fast charging infrastructure are thus hugely invested in by governments and private companies. AC charging stations require an on-board charger (OBC), while DC charging stations move charger power electronics, filters, and so on off board [1]. The charging power of a DC charging station can be much higher than that of an AC charging station with OBC regarding weight and volume constraints. In high-performance electric motorcycle (HPEM) application, weight and volume constraints are much more critical than in other type of EVs. Such vehicles in the market can only be installed with a low-power OBC [2]. This results in a long charge duration. Very few high-performance electric vehicles (HPEVs) have DC charging capability, thus they are less practical in countries where bulky and expensive DC charging stations are not well covered [3].

Integrated charger-inverters (ICI) allow using power electronic components as an inverter in driving mode and can be reconfigured by relays and contactors to be used as a charger in charging mode. Several possibilities have been reviewed, including single-phase input, three-phase input, multi-machine, multi-phase machine, and so on [3–13]. However, for motorcycle applications, only three-phase machines have been reasonably considered owing to their weights and volumes.

In the literature, EVs with several types of three-phase electric motors have been proposed, such as permanent magnet synchronous motors (PMSMs), switched-reluctance motors (SRMs), and induction motors (IMs) [14–16]. PMSM offers high efficiency [14]. SRMs give cost-effective, but poor efficiency and high ripple torque [15,16]. However, most ICI have IMs. This is because of the IMs' advantages, such as low maintenance requirements, reliability, and low cost [14,15].

To use the motor's winding as an inductor for ICI, the motor's torque must be investigated primarily during the charging process, resulting in low efficiency. For the three-phase ICI with a three-phase synchronous machine, special winding must be used to ensure that the average torque is zero [10]. To nullify the averaged torque, another solution is proposed without any additional component in [11], where the four motors have EVs with a three-phase grid as an energy source. Each phase of the grid is connected directly to the neutral point of the motor. Therefore, the currents of each phase flow through the three windings at the same waveform (zero-sequence stator currents) and cancel the field of each other so that there is no torque production. The applicable motor can be either three-phase IMs or three-phase PMSM. This technique can be applied for the single three-phase motor with an extra leg of the inverter [12] or the two three-phase motor without the extra leg [13] with single-phase grid supply. However, these configurations have one main disadvantage, which is the pulsation current at double grid frequency of battery due to the use of a single-phase grid. Another work is proposed in [17], where a single-phase quasi-Z-source rectifier with an active filter is used. With the active filter to absorb the double grid frequency ripple, the dc-link capacitor, inductor, and capacitor of the quasi-Z-source converter can be reduced to gain a low weight and volume benefit. However, this converter requires a sophisticated controller, especially to control the active filter.

To demonstrate that average torque during the charging process is null, several works proposed it mathematically. Recently, finite element results are used to validate the average torque of PMSMs [18]. However, such an analysis is rare for IMs.

This work focuses on a 7 kW ICI for HPEM. Common components are shared in drive and charge modes. Weight, volume, and cost saving can be expected. The charging power of 7 kW is more usable in the real-world situation, where a 10–14 kWh battery pack can be fully charged in approximately 2 h. Moreover, 50 km of range can be topped up within 20 min.

A two-stage ICI for AC induction machine (IM) powertrain with power factor correction (PFC) as well as battery charger functions are investigated in this work. ICI topology and control algorithm are verified using circuit simulations. Finite element analysis (FEA) determines the torque and losses of IM in charge mode. Finally, simulations are conducted and some results are shown in the last section.

2. Integrated Charger-Inverter

2.1. Topology

The proposed ICI is used for a high-performance electric motorcycle (HPEM). The HPEM is equipped with a 100 kW three-phase IM powertrain driven by a three-phase inverter. In charge mode, six power switches from a three-phase full-bridge inverter and IM's phase windings are reconfigured and reused as a line filter, as well as a single-phase bridgeless rectifier with power factor correction (PFC) and a bi-directional buck-boost converter for the battery charger.

Figure 1 shows the topology of the electric powertrain in drive mode. It is a conventional three-phase full bridge inverter. A battery pack is directly connected to the DC bus.

In charge mode, S1, S2, S3, and S4 help reconfigure the topology, as shown in Figure 2. Phase-A winding of IM is used as a line filter. Two half-bridge legs (T1, T2, T3, and T4) are controlled as an AC/DC PFC rectifier. Another half-bridge leg (T5 and T6) functions as bi-directional buck-boost DC/DC converter connected to the battery pack through an additional inductor.

The switches S1, S2, S3, and S4 must be controlled to ensure that they function correctly. For driving mode, S1 and S3 are on, while S2 and S4 are off, as shown in Figure 1. In charging mode, S2 and S4 must be on, while S1 and S3 must be off, as detailed in Figure 2.

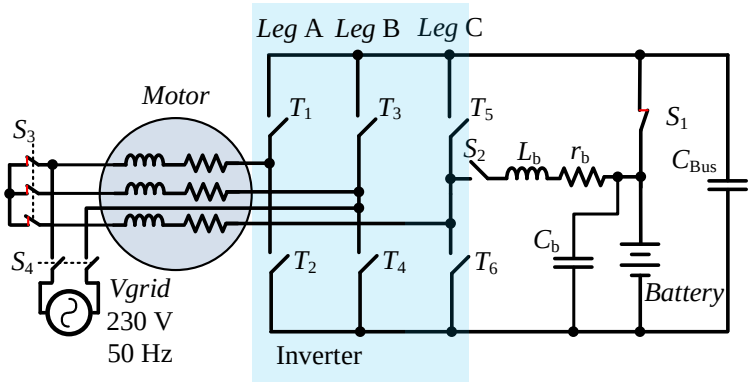

Figure 1. Integrated charger-inverter (ICI) topology in drive mode.

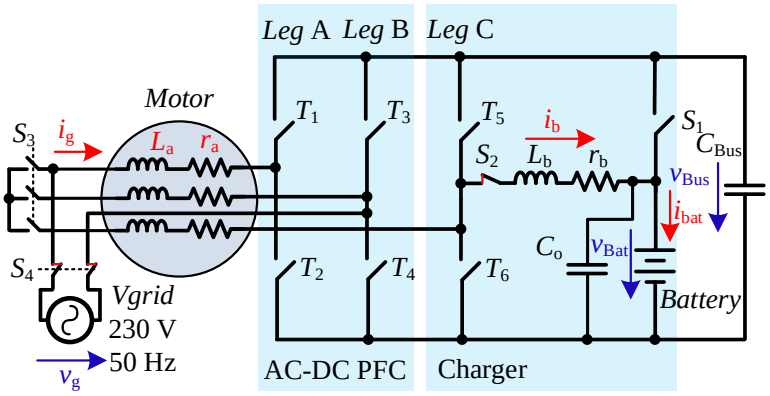

Figure 2. ICI topology in charge mode. PFC, power factor correction.

2.2. Control Algorithm

When the converter system operates in charging mode and supposes that all devices are ideal except inductors (L_a, L_b), which contain parasitic resistances (r_a, r_b), the system can be expressed in the averaged model as follows:

$$L_a \frac{di_g}{dt} = v_g - r_a i_g - d_{PFC} v_{Bus} \quad (1)$$

$$C_{Bus} \frac{dv_{Bus}}{dt} = d_{PFC} i_g - i_b \quad (2)$$

$$L_b \frac{di_b}{dt} = d_{Ch} v_{Bus} - r_b i_b - v_{Bat} \quad (3)$$

$$C_o \frac{dv_{Bat}}{dt} = i_b - i_{bat} \quad (4)$$

where $d_{PFC} \in [-1, 1]$ and $d_{ch} \in [0, 1]$ are duty cycles corresponding to the switch turn-on time during the switching period $T = 1/f_s$ for the PFC and charger, respectively. The voltages v_g and v_{Bus} are the grid and output voltage, where v_{bat} is the battery voltage. i_g and i_b are the grid and battery currents, respectively.

In this article, we consider only the AC-DC PFC converter and battery charger; therefore, control of inverter in driving mode is not considered; it can be found in another article.

PFC rectifier control is done in a traditional way, where the cascade control method is used. There are two control loops: inner-current loop and outer-voltage loop, as shown in Figure 3.

Battery charger control is done using constant current (CC) and constant voltage (CV) modes [6]. These modes can be easily defined using a relay with a hysteresis band $\Delta v_{Bat} = V_{Batref} - v_{Bat}$. When v_{Bat} is too far from V_{Batref}, the charger charges the battery in

CC mode, and otherwise in CV mode. The output from the hysteresis relay is fed into the mode selection block to define the current reference i_{Batref} for the current-control loop. Like for PFC rectifier control, two control loops are used, where an indirect-sliding mode control is used for the inner-current loop [19]; a PI controller is for the outer-voltage loop, as shown in Figure 4. Note that i_{Batref} for the CC mode depends on a specification of battery, whereas the PI controller's parameters K_p and T_i are chosen to make the system stable.

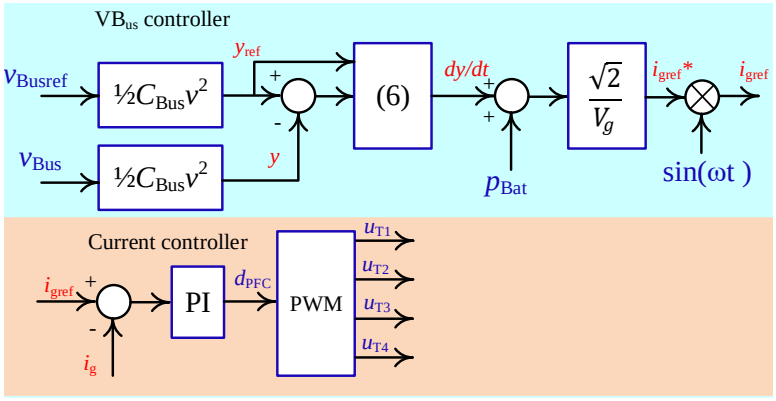

Figure 3. PFC control block diagram.

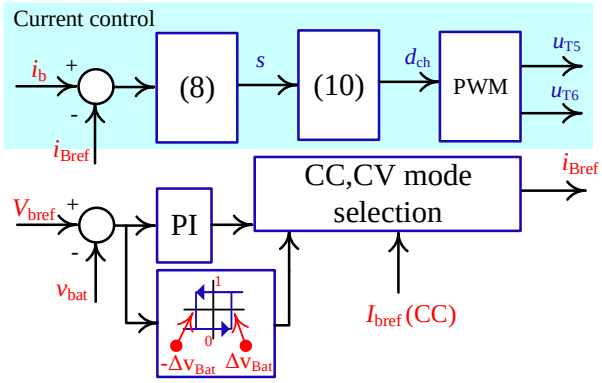

Figure 4. Charger control block diagram. CC, constant current; CV, constant voltage.

To control the output voltage, v_{Bus} and stored energy $y = (1/2)Cv_{Bus}{}^2$ in C_{Bus} are considered [20]. Then, it can be expressed as follows:

$$\dot{y} = C_{Bus} \times v_{Bus} \times \dot{v}_{Bus} = p_{in} - r_g \times i_g{}^2 - p_{Bat} \quad (5)$$

where p_{in} is the input power drawn from the grid and p_{bat} is the load power.

Therefore, the following control law is used to control y constant.

$$\dot{y}_{ref} - \dot{y} + k_1(y_{ref} - y) + k_2 \int (y_{ref} - y)d\tau = 0 \quad (6)$$

The control parameters k_1 and k_2 can be determined referring to a damping factor ξ and angular frequency ω_n of the standard second-order system $F(s) = s^2 + 2\xi\omega_n s + \omega_n{}^2$, so the controlled system is stable.

The input power p_{in} is the power needed for load, and it can be used as a reference for the input-current loop of the PFC. The current reference can be obtained using the peak current value, corresponding to p_{in}, which is nearly a constant multiple of a unit-sinusoidal waveform. Then, it is fed to a PI controller to govern the input current to be a sinusoidal

shape and in phase to the grid voltage. The PI's parameters are determined using a phase margin in a Bode diagram.

$$F_{PI}(s) = K_p + 1/(T_i s) \tag{7}$$

For the charging control, a nonlinear control, an indirect-sliding mode is chosen. This controller must be fast to mitigate fluctuation from both v_{Bus} and circuit-parameter uncertainty. For a controller based on linear analysis, linearization may be used to obtain a model for design purposes. Instead, sliding mode control can use a nonlinear model [18]. For the constant current control, it governs as follows:

$$s = i_b - i_{bref} + K_i \int (i_b - i_{bref}) d\tau \tag{8}$$

with

$$\dot{s} = -\lambda \times s \tag{9}$$

Applying the time derivative result of (8), and then replacing it in (9), we can find d_{ch} for $\forall t\ v_{Bus} > 0$.

$$d_{ch} = \frac{[(-\lambda s + i_{bref} - K_i(i_b - i_{bref})) \times L_b + r_b \times i_b + v_{Bat}]}{v_{Bus}} \tag{10}$$

When the controller controls the system, its pole can be fixed by the value of λ and K_i, e.g., $\lambda = K_i = 2\pi f_s/10$, where f_s is the switching frequency.

3. Component Sizing

According to the topology shown in Figure 2, there are several capacitors and inductors. Their parameter must be carefully selected to suit their needs. The following sections determine their critical values based on the given specifications.

3.1. Inductors

In the PFC rectifier, only one inductor is usually placed in the circuit. Its minimum value is as follows [21]:

$$L_a = \frac{\left(\sqrt{2} \times V_g\right)^2}{4 \times f_s \times P_{Bat}} \tag{11}$$

where $\sqrt{2}V_g$ is the peak input voltage, P_{Bat} is the output power, and f_s is the switching frequency. For the charger, the inductor L_b can be chosen based on the maximum allowable ripple current Δi_b, e.g., 2% [22]:

$$L_b = \frac{V_{Bus}}{4 \times f_s \times \Delta i_b} \tag{12}$$

3.2. Capacitors

In the PFC rectifier without an active filter, only one capacitor is usually placed in the DC link. Its minimum capacitance can be computed as in (13) [23].

$$C_{Bus} = \frac{P_{Bat}}{2\pi \times f_{grid} \times V_{Bus} \times \Delta V_{Bus}} \tag{13}$$

where f_{grid} is the grid frequency; ΔV_{Bus} is the peak-to-peak ripple voltage around the desired output voltage V_{Bus}, e.g., ΔV_{Bus} = 25%, according to the parameters given in Table 1; and C_{Bus} has a minimum of 557 µF for P_{Bat} = 7 kW power requirement compared with 400–600 µF found in conventional OEM HEV/EV 100 kW inverters without an ICI feature. However, the ripple voltage ΔV_{Bus} does not cause any problem to the quality of charging current thanks to the high-band width nonlinear current controller; the controller rejects the ripple effect. For the capacitor across the battery C_o, it is used to absorb the ripple

current of the battery current. The maximum ripple voltage Δv_{Bat}, e.g., 1% can be used to determine the value of C_o as follows [22]:

$$C_o = \frac{V_{Bus}}{32\Delta v_{Bat} L f_s{}^2} \quad (14)$$

3.3. Specific Power Comparison

Table 1 shows the OBC parameters from articles and OEM manufacturers. Specific weight and power density can be varied from 0.41 to 1.1 kW/kg and from 0.61 to 2 kW/L. The OBC cost in 2014 is approximately 83 USD/kW.

Table 1. On-board charger (OBC) parameters.

Manufacturer/Reference	Specific Power (kW/kg)	Power Density (kW/L)	Cost Per kW (USD/kW)
2012 Nissan Leaf 6.6 kW OBC [24]	0.41	0.66	N/A
Tier one OBC 3.3 kW [24]	N/A	N/A	83
Eton (1)	N/A	2	N/A
Ovartech 6.6 kW Water-cool (2)	1.1	0.61	N/A

(1) https://www.eaton.com/us/en-us/catalog/emobility/on-board-charger.specifications.html. (2) https://www.ovartech.com/?product=on-board-6-6kw-liquid-cooled-charger-200-420vdc.

Table 2 shows the estimated weight, volume, and cost of the proposed 7 kW integrated charger-inverter. It must be noted that the main components, shown in Table 2, are added to a conventional traction inverter so that the whole system can function as a charger. The main traction inverter itself is considered as an existing component in the vehicle and will contribute to achieve the ICI's feature without any additional weight, volume, and cost to the system. As a result, the additional components of the proposed ICI will add approximately 1.19 kg, 0.64 l, and 75 USD to the system. The specific weight, power density, and cost per kW can be computed as 5.88 kW/kg, 10.93 kW/L, and 10.71 USD/kW, respectively. These values are much better than a conventional OBC.

Table 2. Additional components of the proposed integrated charger-inverter 7 kW.

Manufacturer/Reference	Weight (kg)	Volume (L)	Cost (USD)
S2 (40 A, 450 V DC contactor) (3)	0.15	0.11	30
S3 (10 A, 250 Vac 3-pole relay) (4)	0.03	0.02	10
L_b (estimated)	1	0.5	30
C_o (3 uF, 450 V) (5)	0.0085	0.0074	5
Total	1.19	0.64	75

(3) https://cotronics.nl/product/gpr040/. (4) http://www.farnell.com/datasheets/1993447.pdf. (5) https://www.mouser.vn/ProductDetail/Vishay-Roederstein/MKP1848530454K2.

Compared with the 6.6 kW integrated charger-inverter found in [25], it will add weight of 1.6 kg to the conventional traction inverter, which is equivalent to 4 kW/kg specific weight, as shown in Table 3. This value is quite similar to the one of the proposed ICI.

Table 3. Integrated charger-inverter (ICI) parameters.

Manufacturer/Reference	Specific Power (kW/kg)	Power Density (kW/L)	Cost Per kW (USD/kW)
Proposed ICI 7.7 kW	5.88	10.93	10.71
ICI 6.6 kW from [25]	4	N/A	N/A

4. Simulation Results

4.1. Charge Simulations

Simulations were conducted in PSIM and MATLAB/Simulink environment using the parameters given in Tables 4 and 5. Circuit components were simulated in PSIM and coupled with control algorithms running in MATLAB/Simulink.

Figure 5 shows the results in steady state for P_{Bat} = 7 kW. The output voltage v_{Bus} contains ripple voltage Δv_{Bus} of about 96.5 V, which is 24% of the reference voltage.

In Figure 6, one cycle of the grid voltage v_g and grid current i_g is illustrated. i_g is multiplied by 4 to increase its amplitude; it is close to the sinusoidal wave; therefore, the system draws power from the grid with a high power factor. It can be seen from Figure 7 that PF is higher than 0.8 at the light-load condition. It reaches 0.998 when the output power is higher than 6 kW.

Table 4. Converter parameters. PFC, power factor correction.

Parameters (Unit)	
Grid voltage, V_g	230 Vrms
Grid frequency, f_{grid}	50 Hz
Switching frequency, f_s	20 kHz
Output voltage, V_{Bus}	400 V
Maximum battery power, p_{Bat}	7 kW
PFC inductor L_a, r_a (phase a winding)	1.3 mH, 0.015 Ω
Charger inductor L_b, r_b (additional inductor)	10 mH, 0.015 Ω
Capacitor, C_{Bus}	640 μF
Capacitor, C_o	2.2 μF
Battery full voltage of 48 cells	201.6 V

Table 5. Control parameters.

Parameters (Unit)	
PFC	
- K_P, T_i	0.11, 0.5 ms
- ξ, ω_n	0.707, 150 rad/s
- K_1, K_2	212.10, 22,500
Charger	
- $\lambda = K_i$	$2\pi f_s/10$ rad/s
- K_P, T_i	0.01, 0.1 s

Figure 5 shows results in steady state for $P_{Bat} = 7$ kW. The output voltage contains ripple voltage of about 96.5 V, which is 24% of the reference voltage, and the grid current is illustrated, which is multiplied by 4 to increase its amplitude; it is close to the sinusoidal wave; therefore, the system draws power from the grid with a high power factor. It can be seen from Figure 7 that PF is higher than 0.8 at the light-load condition. It reaches 0.998 when the output power is higher than 6 kW. Figures 8–10 show the responses of the system when P_{Bat} is changed slightly from 1.5 kW to 7 kW. The rate of current reference is limited to four times less than V_{Bus}/L_b to ensure that the system can be adequately worked without any overshoot of the battery current, as shown in Figure 8. The waveform of battery current shows that the high-band width nonlinear current controller can effectively reject the ripple effect from v_{Bus}.

From the results, the output voltage v_{Bus} quickly returns to its reference after the change of the battery current, while the grid current is in good shape. A monotonic relationship between Δv_{Bus} and the grid current can be observed.

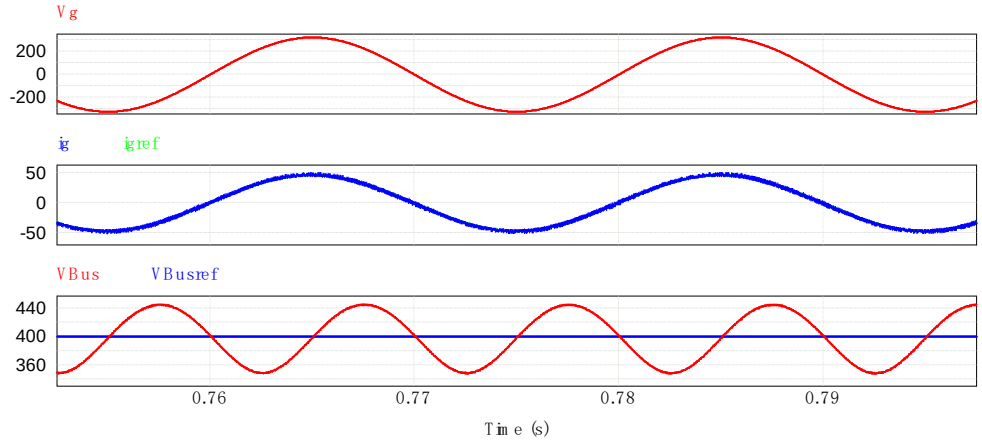

Figure 5. DC link voltage without active filter for $P_{Bat} = 7$ kW.

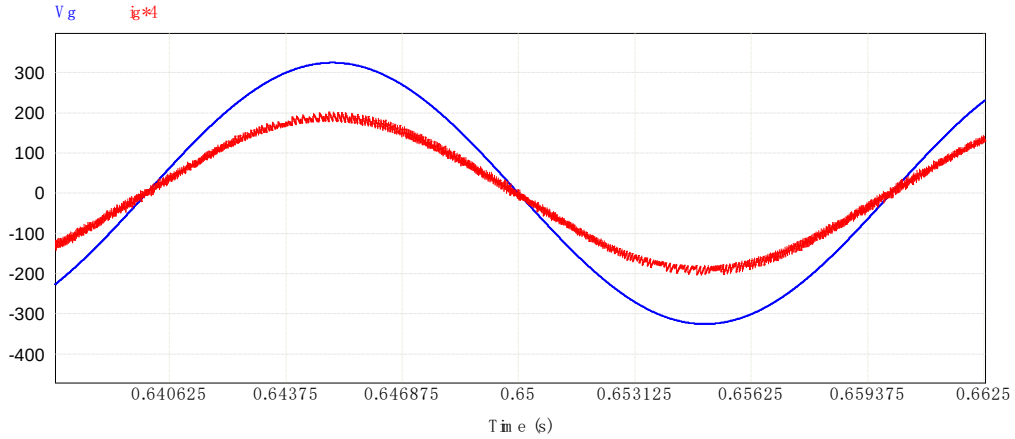

Figure 6. Input current waveform for $P_{Bat} = 7$ kW.

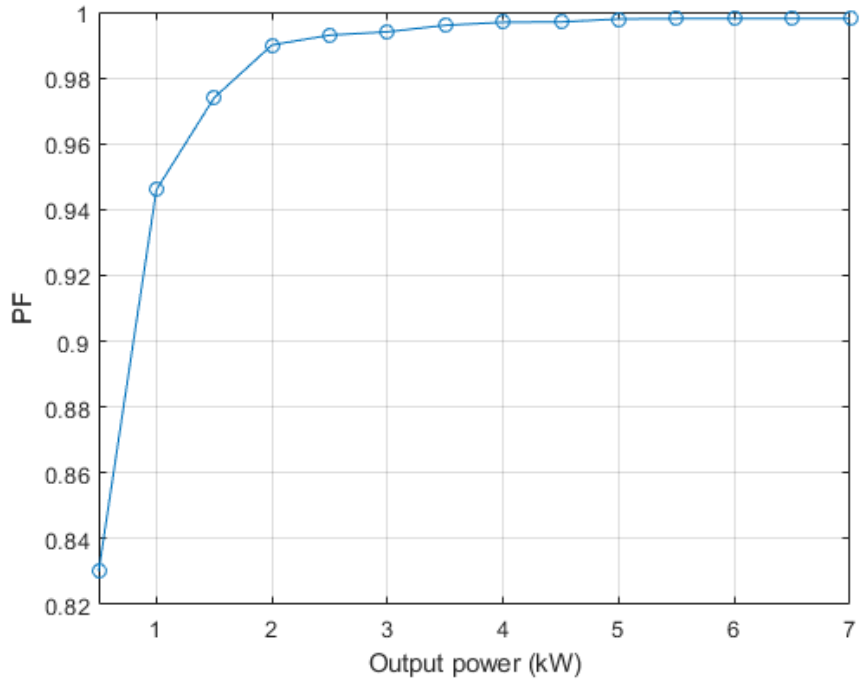

Figure 7. Power factor (PF) for different levels of output power.

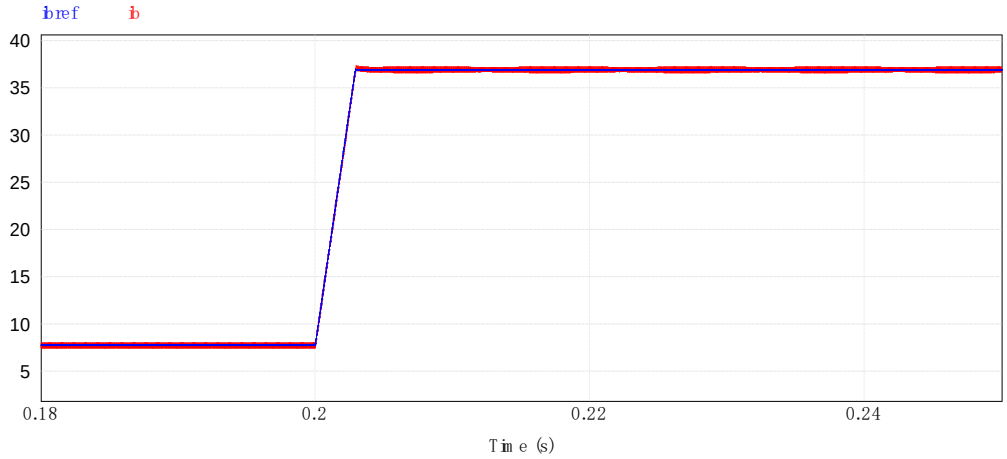

Figure 8. Battery current waveform for $P_{Bat} = 1.5\ kW \rightarrow 7\ kW$.

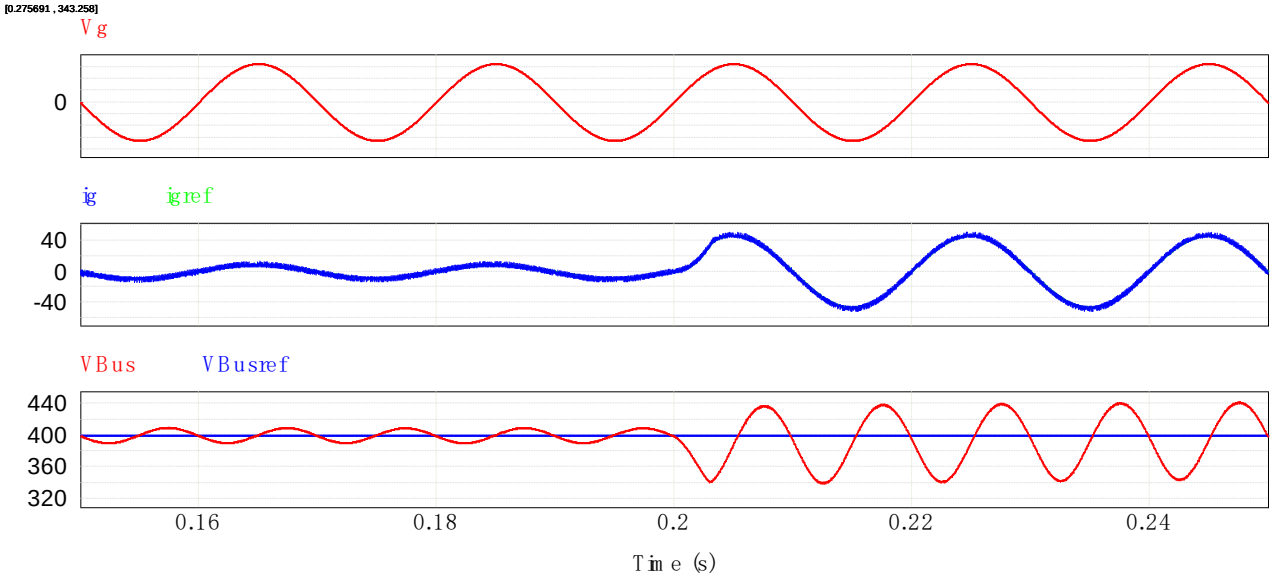

Figure 9. DC link voltage without an active filter $P_{Bat} = 1.5\ kW \rightarrow 7\ kW$.

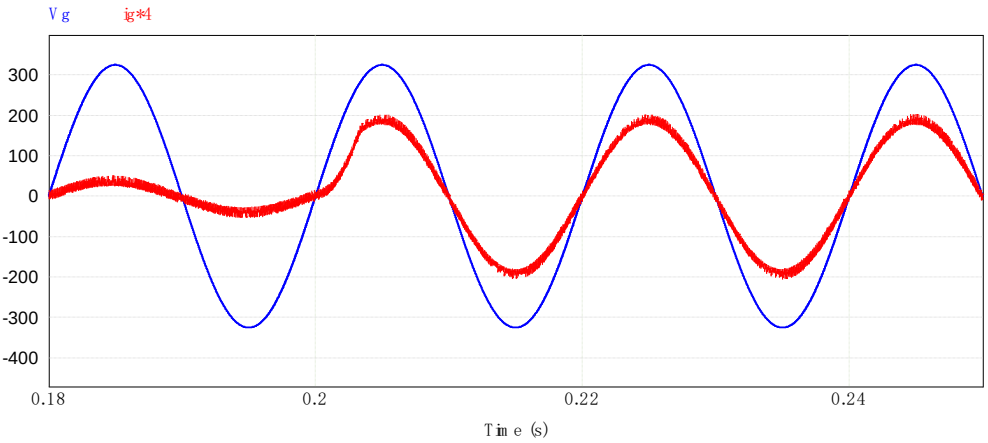

Figure 10. Input current waveform for $P_{Bat} = 1.5\ kW \rightarrow 7\ kW$.

4.2. Electromagnetic Torque

In charge mode, one motor winding is reused as a line filter inductor, as shown in Figure 2. The input current passing through the winding may generate torque. While simple equations can be computed to quantify the electromagnetic torque, finite element analysis (FEA) gives more information on flux distribution and losses in the machine.

The first simulation in 2D FEA is realized with the hypothesis of sinusoidal current input of 32 Arms. Figure 11 shows the electromagnetic torque stabilized in 100 ms, where the average value is only 7.7 mNm. This torque level cannot move the electric motorcycle. The losses calculated in 2D FEA without taking into account the end winding are presented in Figure 12. Their values are very small. Thermal calculation is not necessary for this motor.

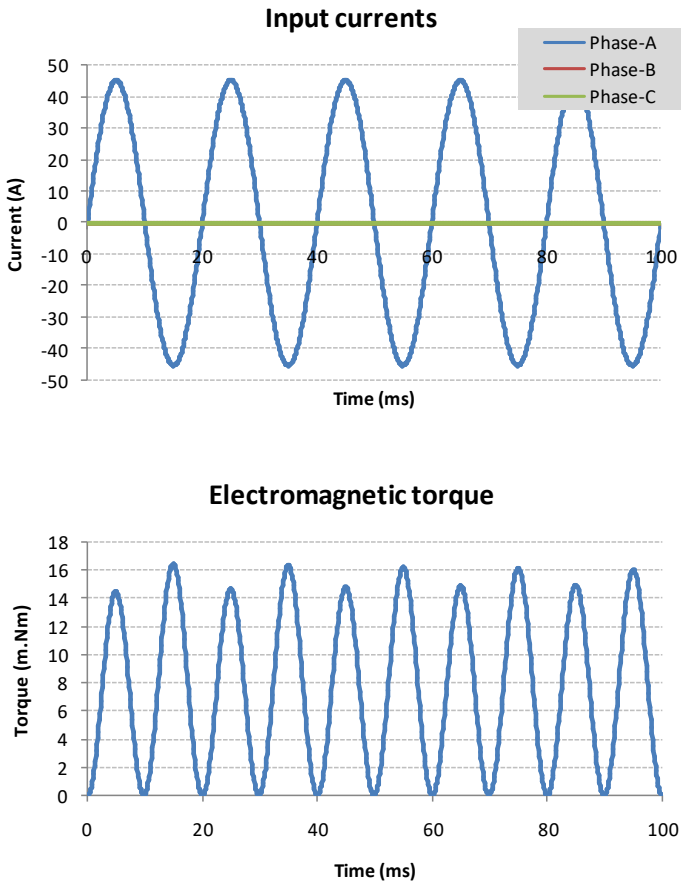

Figure 11. Electromagnetic torque with 32 A sinusoidal current input.

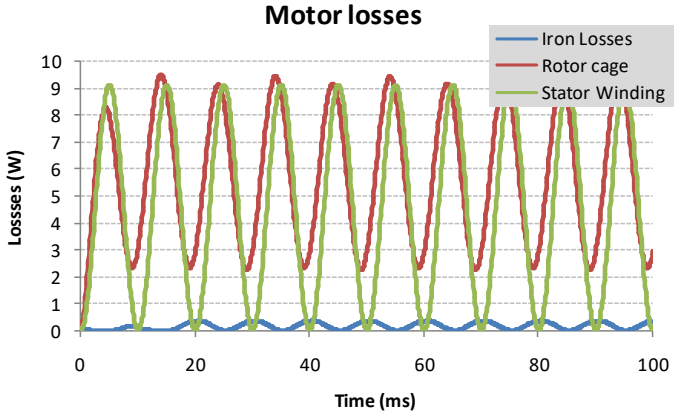

Figure 12. Losses of induction motor in 2D finite element analysis (FEA).

The second modeling of the machine in 2D FEA is done in a more realistic case. The harmonic 5 and 7 are taken into account in the input current. The results are shown in Figures 13–15. The electromagnetic torque is stabilized for eight times longer than the first simulation with sinusoidal current input. Even with adding the current harmonics 5 and 7, the average electromagnetic steady-state torque is only 16 mNm, and the losses do not impact the thermal behavior of the machine.

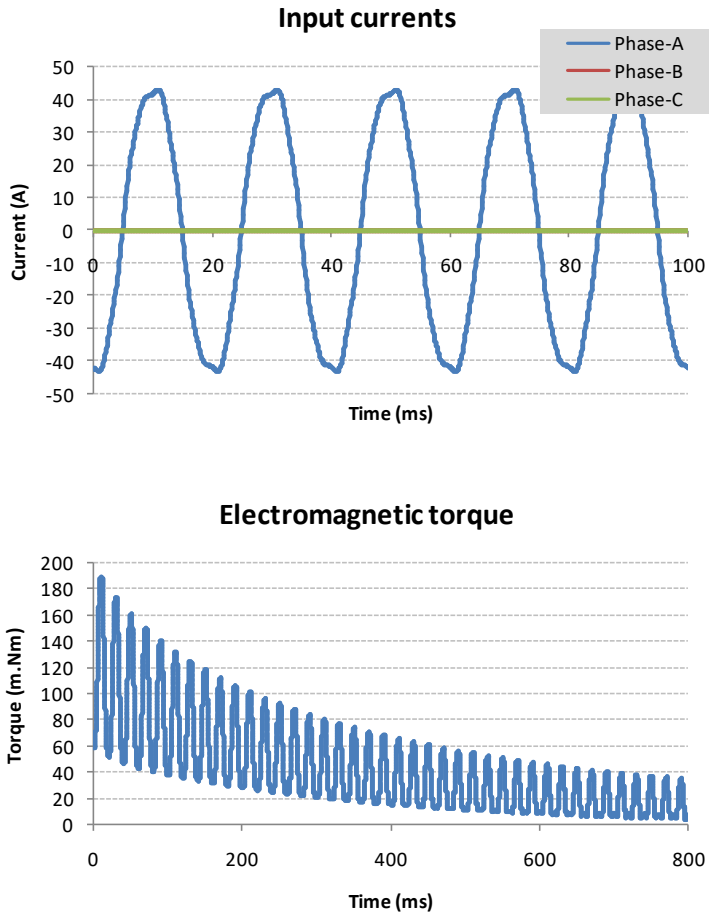

Figure 13. Electromagnetic torque with 32 A harmonic current.

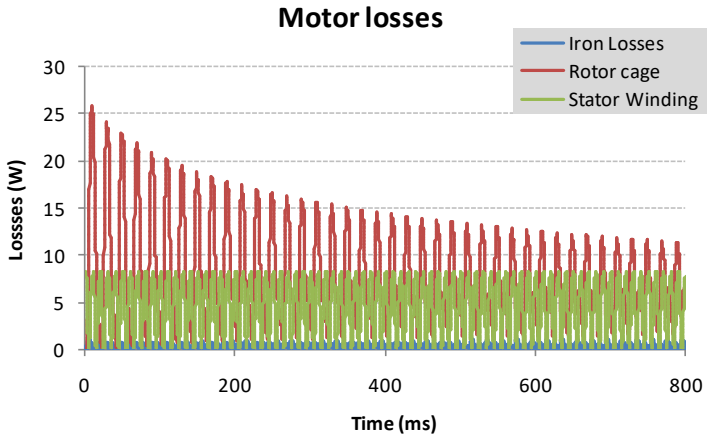

Figure 14. Losses in 2D FEA with harmonic current.

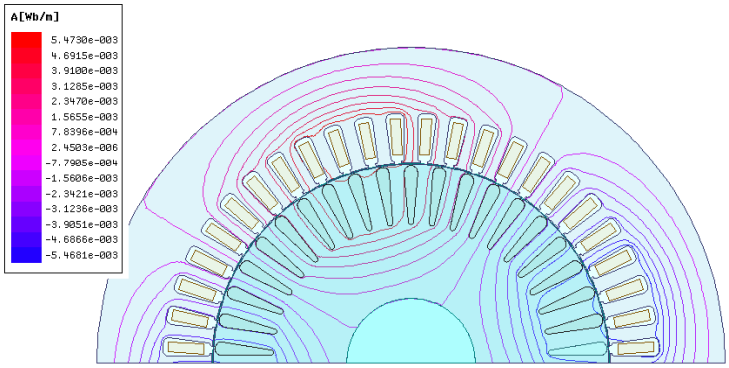

Figure 15. Flux circulation of induction motor (IM) in charge mode.

5. Conclusions

An integrated charger-inverter (ICI) with an induction motor for high-performance electric motorcycle is proposed. To reduce the weight, volume, and cost, the main components are shared in drive and charge modes. The phase-A winding is used as an inductor for PFC using the first two legs of the three-phase inverter, while another leg is utilized to act as a charger with an additional inductor. The high bandwidth nonlinear controller rejects the double frequency ripple on the dc-link and allows the charger to adequately provide a constant current or constant voltage charging. The simulation results of 7 kW system validate the proposed system. Finite element analysis (FEA) determines the torque and losses of IM in charging mode and reveals that the torque productions are very small. It is notable to move the rotor. In addition, losses of the motor from the FEA results are low. Therefore, the proposed system can be implemented further.

Author Contributions: This article presents the collective work of all authors (V.T.T., M.P., and S.K.). All authors have read and agreed to the published version of the manuscript.

Funding: This work was funded in part by Hanoi University of Science and Technology (HUST) and King Mongkut University of Technology north of Bangkok, Thailand (grant number KMUTNB-63-KNOW-035).

Conflicts of Interest: The authors declare no conflict of interest.

References

1. Drobnic, K.; Grandi, G.; Hammami, M.; Mandrioli, R.; Ricco, M.; Viatkin, A.; Vujacic, M. An Output Ripple-Free Fast Charger for Electric Vehicles Based on Grid-Tied Modular Three-Phase Interleaved Converters. *IEEE Trans. Ind. Appl.* **2019**, *55*, 6102–6114. [CrossRef]
2. Patil, D.; Agarwal, V. Compact Onboard Single-Phase EV Battery Charger with Novel Low-Frequency Ripple Compensator and Optimum Filter Design. *IEEE Trans. Ind. Appl.* **2016**, *65*, 1948–1956. [CrossRef]
3. Shi, C.; Tang, Y.; Khaligh, A. A Three-Phase Integrated Onboard Charger for Plug-In Electric Vehicles. *IEEE Trans. Power Electron.* **2018**, *33*, 4716–4725. [CrossRef]
4. Hatti, N.; Nuilers, S.; Chayopitak, N.; Somsiri, P. An integrated battery charger configuration for SRM drive in electric motorcycles. *IEEJ Trans. Electr. Electron. Eng.* **2018**, *13*, 295–302. [CrossRef]
5. Subotic, I.; Bodo, N.; Levi, E. Single-Phase On-Board Integrated Battery Chargers for EVs Based on Multiphase Machines. *IEEE Trans. Power Electron.* **2016**, *31*, 6511–6523. [CrossRef]
6. Shi, C.; Tang, Y.; Khaligh, A. A Single-Phase Integrated Onboard Battery Charger Using Propulsion System for Plug-in Electric Vehicles. *IEEE Trans. Veh. Technol.* **2017**, *66*, 10899–10910. [CrossRef]
7. Cheng, H.; Wang, Z.; Yang, S.; Huang, J.; Ge, X. An Integrated SRM Powertrain Topology for Plug-In Hybrid Electric Vehicles with Multiple Driving and Onboard Charging Capabilities. *IEEE Trans. Transp. Electrif.* **2020**, *6*, 578–591. [CrossRef]
8. Bodo, N.; Levi, E.; Subotic, I.; Espina, J.; Empringham, L.; Johnson, C.M. Efficiency Evaluation of Fully Integrated On-Board EV Battery Chargers with Nine-Phase Machines. *IEEE Trans. Energy Convers.* **2017**, *32*, 257–266. [CrossRef]
9. Metwly, M.Y.; Abdel-Majeed, M.S.; Abdel-Khalik, A.S.; Hamdy, R.A.; Hamad, M.S.; Ahmed, S. A Review of Integrated On-Board EV Battery Chargers: Advanced Topologies, Recent Developments and Optimal Selection of FSCW Slot/Pole Combination. *IEEE Access* **2020**, *8*, 85216–85242. [CrossRef]

10. Kataoka, R.; Shichi, A.; Yamada, H.; Iwafune, Y.; Ogimoto, K. Comparison of the Economic and Environmental Performance of V2H and Residential Stationary Battery: Development of a Multi-Objective Optimization Method for Homes of EV Owners. *World Electr. Veh. J.* **2019**, *10*, 78. [CrossRef]
11. Subotic, I.; Jones, M.; Levi, E. A fast on-board integrated battery charger for four-motor EVs. In Proceedings of the 2014 International Conference on Electrical Machines (ICEM), Berlin, Germany, 2–5 September 2014; pp. 2066–2072.
12. Thimmesch, D. An SCR inverter with an integral battery charger for electric vehicles. *IEEE Trans. Ind. Appl.* **1985**, *IA-21*, 1023–1029. [CrossRef]
13. Tang, L.; Su, G.-J. Control scheme optimization for a low-cost, digitally-controlled charger for plug-in hybrid electric vehicles. In Proceedings of the 2010 IEEE Energy Conversion Congress and Exposition, Atlanta, GA, USA, 12–16 September 2010; pp. 3604–3610.
14. Matsuhashi, D.; Matsuo, K.; Okitsu, T.; Ashikaga, T.; Mizuno, T. Comparison study of various motors for EVs and the potentiality of a ferrite magnet motor. *IEEJ J. Ind. Appl.* **2015**, *4*, 173–179. [CrossRef]
15. Tuan, V.T.; Kreuawan, S.; Somsiri, P.; Tungpimolrut, K.; Huy, P.N. Switched Reluctance Motor and Induction Machine for E-Scooter Based on Driving Cycles Design Comparisons. *IEEJ Trans. Electr. Electron. Eng.* **2020**, *15*, 931–938. [CrossRef]
16. Vosswinkel, M.; Lohner, A.; Platte, V.; Hirche, T. Design, Production, and Verification of a Switched-Reluctance Wheel Hub Drive Train for Battery Electric Vehicles. *World Electr. Veh. J.* **2019**, *10*, 82. [CrossRef]
17. Na, T.; Zhang, Q.; Tang, J.; Wang, J. Active power filter for single-phase Quasi-Z-source integrated on-board charger. *CPSS Trans. Power Electron. Appl.* **2018**, *3*, 197–201. [CrossRef]
18. Xiao, Y.; Liu, C.; Yu, F. An Effective Charging-Torque Elimination Method for Six-Phase Integrated On-Board EV Chargers. *IEEE Trans. Power Electron.* **2020**, *35*, 2776–2786. [CrossRef]
19. Gavagsaz-Ghoachani, R.; Saublet, L.; Phattanasak, M.; Martin, J.; Nahid-mobarakeh, B.; Pierfederici, S. Active stabilisation design of DC–DC converters with constant power load using a sampled discrete-time model: Stability analysis and experimental verification. *IET Power Electron.* **2018**, *11*, 1519–1528. [CrossRef]
20. Gavagsaz-Ghoachani, R.; Phattanasak, M.; Martin, J.; Nahid-Mobarakeh, B.; Pierfederici, S. A Fixed-Frequency Optimization of PWM Current Controller—Modeling and Design of Control Parameters. *IEEE Trans. Transp. Electrif.* **2018**, *4*, 671–683. [CrossRef]
21. Das, P.; Pahlevaninezhad, M.; Moschopoulos, G. Analysis and Design of a New AC–DC Single-Stage Full-Bridge PWM Converter with Two Controllers. *IEEE Trans. Ind. Electron.* **2013**, *60*, 4930–4946. [CrossRef]
22. Ferrieux, J.P.; Forest, F. *Alimentations à Découpage Convertisseurs à Résonance*, 3rd ed.; Dunod: Malakoff, France, 2006.
23. Nussbaumer, T.; Raggl, K.; Kolar, J.W. Design Guidelines for Interleaved Single-Phase Boost PFC Circuits. *IEEE Trans. Ind. Electron.* **2009**, *56*, 2559–2573. [CrossRef]
24. Shenai, K. WBG Power Converters for Hybrid & EV Applications. *Auto Tech. Rev.* **2016**, *5*, 42–47.
25. Robert, E.; Dragan, M.; Khurram, A.; David, J.; Daniel, F.; Hyeokjin, K.; Usama, A.; Jianglin, Z.; Kraig, O.; Brandon, P.; et al. *A Disruptive Approach to Electric Vehicle Power Electronics Final Report*; Univ. of Colorado: Boulder, CO, USA, 2017.